Mirror to measure Small Angle X-ray Scattering signal in high energy density experiments

Smid, M.; Bähtz, C.; Laso García, A.; Göde, S.; Grenzer, J.; Kluge, T.; Konôpková, Z.; Makita, M.; Pelka, A.; Prencipe, I.; Preston, T.; Rödel, M.; Cowan, T.;

Originally published:

December 2020

Review of Scientific Instruments 91(2020), 123501

DOI: https://doi.org/10.1063/5.0021691

Mirror to measure Small Angle X-ray Scattering signal in high energy density experiments

M. Šmíd,[1, a)] C. Baehtz,[1] A. Pelka,[1] A. Laso García,[1] S. Göde,[2] J. Grenzer,[1] T. Kluge,[1] Z. Konopkova,[2] M. Makita,[2] I. Prencipe,[1] T. R. Preston,[2] M. Rödel,[1] and T. E. Cowan[1]
[1)]*Helmholtz Zentrum Dresden Rossendorf, Dresden, 01328, Germany*
[2)]*European XFEL, Schenefeld, 22869, Germany*

(Dated: 7 December 2020)

Small angle x-ray scattering (SAXS) is a well established technique to detect nanometer scale structures in matter. In a typical setup, this diagnostic uses a detector with a direct line of sight to the scattering target. However, in the harsh environment of high intensity laser interaction, intense secondary radiation and high-energy particles are generated. Such a setup would therefore suffer a significant increase of noise due to this background, which could eventually prevent such measurement. In this paper, we present a novel tool consisting of a mosaic graphite crystal which works as a mirror for the SAXS signal and allows us position the detector behind appropriate shielding. This paper studies the performance of this mirror both by experiment at the European XFEL (X-Ray Free-Electron Laser Facility) laboratory and by simulations.

I. INTRODUCTION

Small angle x-ray scattering (SAXS) is a diagnostic technique where the x-ray beam is scattered to small angles of order of 10-100 mrad. It is used to measure electron spatial distribution structures in order of $10 - 100$ nm. It is a well established technique at synchrotrons and x-ray free electron lasers (XFELs)[1,2]; recently, it has been used to study high intensity laser plasma interactions[3]. In this case, the scattering target is directly heated by a high intensity optical laser and therefore a significant amount of radiation and high energy particles are produced. This broadband divergent radiation increases the background (noise) level on the SAXS detector. The electromagnetic pulse (EMP) can also create issues with the electronics of the detector. Therefore, with the increasing performance of available lasers, the usage of such diagnostics with direct line of sight to the target might suffer from low signal / noise ratio. This led us to develop a new instrument described in this paper. Though its geometrical principles are very similar to a monochromator with Rowland circle geometry, its main purpose is to deflect the SAXS signal and therefore we call it the *SAXS mirror*.

XFELs with a photon energy of 5 to 25 keV, with pulse duration of tens of femtoseconds and brightness sufficient to provide single shot measurement are excellent tools to study laser matter interaction in pump probe setups. The HED (High Energy Density) instrument at the European XFEL (Hamburg, Germany)[4] is a unique platform dedicated to perform these types of experiments. Within this instrument, the HiBEF user consortium is building both the high intensity laser (300 TW titanium sapphire system with duration 25 fs) and high energy laser (100 J class Neodymium-glass based laser), which will be used to heat (pump) the matter. The SAXS mirror described in this paper was designed especially to perform SAXS measurements on matter driven by these lasers, and the experimental results shown here were produced in September 2019 during the commissioning beam time number 2554.

SAXS, as a technique, has different variants: GISAXS[5] (Grazing incidence SAXS) is actually a reflection of the x-ray beam from a target at a shallow angle, and with slight modification our mirror could be utilised for this case as well. Resonant SAXS[6] combines x-ray scattering with x-ray absorption on various x-ray resonant transitions, and would benefit from using this instrument without any modification.

HAPG crystals (Highly Annealed Pyrolytic Graphite) are one of the most common mosaic crystals used for x-ray instruments. Mosaic crystals in general are composed of a number of nearly perfect crystallites (or crystal regions) with, to some extent, random orientation with respect to each other and to the crystal surface[7]. The angular distribution between the diffraction vector of a given lattice plane of the different crystallites can be described as Lorentzian, where its FWHM (Full width at half maximum) is called the mosaicity, denoted as m. These crystals are typically used in spectrometers or monochromators, where the mosaicity ensures extremely high efficiency of those instruments compared to those with single crystals. For the case described in this paper, the mosaic structure is used to provide a different benefit: The geometry of the instrument does not allow to have all divergent rays impinging the surface at the same incidence angle. The larger mosaicity translates to the larger acceptance angle of rays with given energy and therefore ensures that x-rays can be reflected over the whole surface of the crystal.

This paper presents the concept of a cylindrically bent *SAXS mirror* instrument, shows the first measured data and compares those to results of raytracing simulations. It discusses several aspects of the instrument that help evaluate whether it is suitable for various prospective experiments. The paper also suggests a suitable workflow to be used to evaluate future data. The codes written to perform this analysis are available upon request to the author.

[a)]Electronic mail: m.smid@hzdr.de

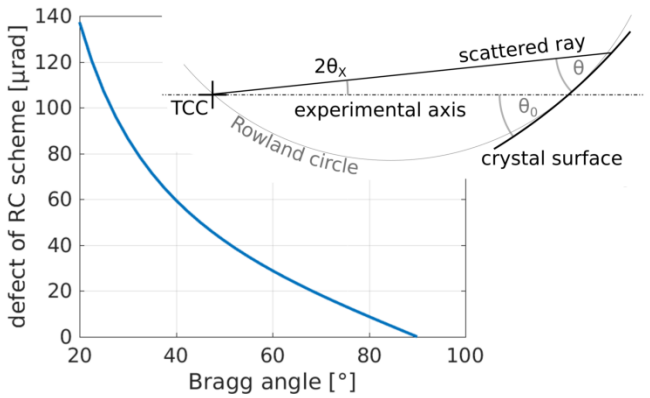

FIG. 1. Defect of the Rowland Circle scheme $\theta - \theta_0$, i.e. the deviation of the angle of incidence of a beam with angular width $2\theta_X = 10$ mrad from the central Bragg angle θ_0. The inset shows the geometry of the scenario.

II. CONCEPT

In this section, the overall design constraints of this instrument are presented including the path which led to the selection of HAPG crystal. The requirements for the mirror are such that it has to reflect a monochromatic x-ray signal originating at single point, the scattering target. (This target is located in the target chamber center, therefore a common abbreviation 'TCC' is used to further denote this point.) Due to the generally low intensity of the scattering signal, a very high reflectivity of the mirror is required, while the distance between TCC and the mirror should be relatively large to avoid damage by possible debris from the target.

Elements considered for such a mirror were the multilayer mirrors (ML), monocrystals, or mosaic crystals. All these follow the Bragg law, which states that the incidence angle of each ray on its surface has to be within a given range from the optimal Bragg angle, further denoted as θ_0. The only shape of surface, where the incidence angle is the same for all rays originating from a single point, is the logarithmic spiral. However, we have concluded that an optical element with such a complicated shape might be close to impossible to be precisely manufactured and aligned. If this shape is substituted by a circle, (which means using the Rowland circle geometry[8]), some deviations in the incidence angle are introduced. This deviation of the Rowland circle scheme is strongly dependent on the incident Bragg angle, but surprisingly it is not a function of the radius of the crystal. Figure 1 illustrates this deviation for a ray horizontally inclined to the experimental axis by 10 mrad.

For typical monocrystals, the rocking curve width, i.e., the range of accepted angles, is typically around 20 - 150 µrad. As these values are close to the variation of the incidence angle shown in Fig. 1, this design would be very tight in precision and manufacture. To use these, we would have to design for higher Bragg angles, and still the setup would suffer from very limited bandwidth and bandwidth variation over the crystal surface.

When using a HAPG crystal with mosaicity $m = 0.1^\circ \approx 1570$ µrad, this defect becomes negligible. On the other hand, due to the random nature of the crystallites, the reflected ray is vertically divergent, and therefore the resolution of the instrument is decreased. Furthermore, the mosaic structure of these crystals requires high precision flat fielding due to a variation in their reflectivity.

Multilayer mirrors (ML), which are widely used as x-ray optics, offer another way to avoid this obstacle. These are formed by a strict periodical arrangement of two layers with high and low electron density materials and very smooth interfaces like for example Pd/B4C. This one-dimensional perfect arrangement can reflect x-rays based on the Bragg equation at incident angles lower than 3°. With current technologies it is possible to produce a ML mirror with linearly varying grating period. This linear variation would very precisely compensate for the different incidence angle. The deviation of the incidence angle from the *local* θ_0 might then be on the level of ≈ 20 µrad, which is sufficiently below their typical rocking curve width. Nevertheless, the very low incidence angle on the order of 1° pushes the design to have a ML mirror very close to TCC, making it vulnerable to target debris. This is especially not optimal due to their higher price.

Based on these considerations, the solution with HAPG mirror was selected to be pursued. The setup was designed to fit into the IC1 chamber of the HED instrument. This chamber extends approximately 1300 mm downstream from TCC to the exit flange of the XFEL beam. The debris issue requires as large distance from TCC to the crystal as possible. The HAPG crystal introduces spread of the rays, which (as described further) translates to a decrease of the angular resolution of the instrument, which is proportional to the crystal-detector distance. Both these constraints motivates us to position the mirror as far downstream as possible, therefore keeping the distance between the detector (located outside of the chamber) and the mirror very low (≈ 250 mm). This makes the whole instrument compact, making it possible to mount it on a single exit flange and keeping it as a single module, which could be used in various experiments without colliding with other instruments.

This setup is shown in Fig. 2. This design is calculated for an x-ray energy of 8150 eV and uses a 120 mm long cylindrically-bent HAPG crystal with a radius of curvature of 5.5 m. The mirror is composed of two separate blocks located symmetrically below and above the beam, letting the XFEL beam pass through the gap to be further used downstream for additional diagnostics or safely dumped.

III. EXPERIMENT

The experiment was performed in the IC1 chamber at the HED instrument of the European XFEL. Two blocks of HAPG crystals were used, each one 12 cm long, 2 cm wide with a 1D curvature of radius 5.5 m along the longer dimension. A 40 µm thick layer of HAPG was deposited onto a 20 mm thick optical glass substrate. Both blocks were mounted within the same holder with a 3 mm wide gap for the XFEL beam. The

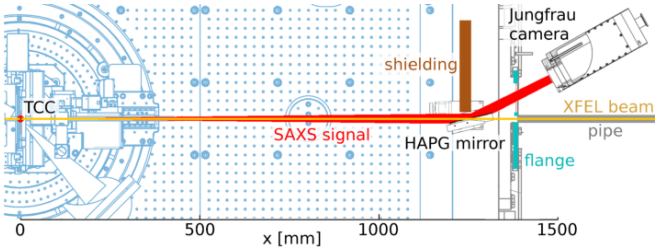

FIG. 2. Schematics of the SAXS mirror instrument located in the IC1 chamber of the European XFEL. Light blue background represents an optical table and a target tower in the chamber. The XFEL beam (orange) is being scattered on a target at TCC, the scattering signal (red) is propagating downstream towards the rear part of the chamber, where it is reflected to the detector by the HAPG mirror. The detector is located outside of the chamber behind a kapton window. The XFEL beam propagates through a gap between the two parts of the crystal further downstream, where it might be used for further diagnostics before reaching the beam dump

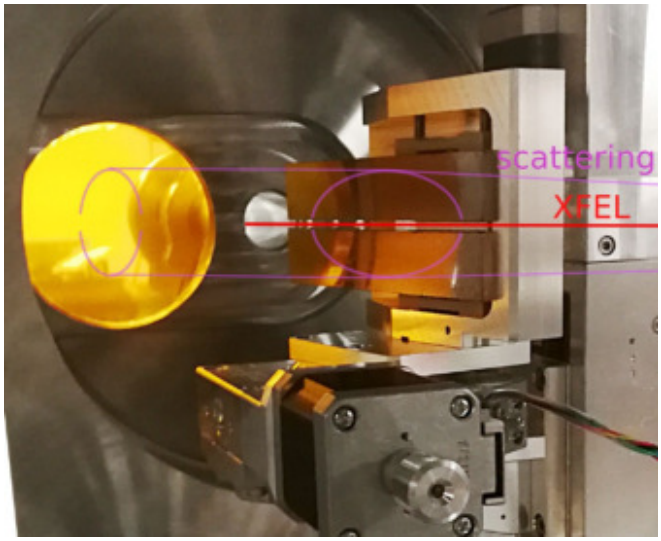

FIG. 3. Photograph of the SAXS mirror located in the IC1 chamber. The XFEL beam and a scattering signal are drawn in red and purple colors, respectively.

crystals were aligned on a motorized 3-axis translation and 1 axis rotation stage, with the center of the crystals located 1230 mm from TCC. A photograph of the crystal in the IC1 chamber is shown in Fig. 3. The direct x-ray beam propagated further downstream in a 2 cm diameter pipe, while the reflected signal went through a kapton window onto a Jungfrau detector. This enables the usage of the direct XFEL beam passing through the gap between the crystals for e.g. sample alignment, PCI imaging etc. The distance between the center of the crystals and the detector chip was 217 mm. The Jungfrau detector has a pixel size of 75 µm and overall chip size 35×70 mm.

A collimated XFEL beam was used, i.e. without focusing optics in the beampath. The size of the beam was limited by closing the entrance slits to 0.5×0.5 mm. In most cases, the beam was attenuated to a factor of 1.04×10^{-5} of its full intensity to prevent damage to the sample and the required photon counts for the data was acquired by accumulation over a few thousand pulse trains containing 1 or 2 bunches per train. Unless otherwise specified, the photon energy of the beam was $E = 8150$ eV and the SASE spectrum was used with bandwidth of approximately 16 eV. The mirror was used at the Bragg angle:

$$\theta_0 = \arcsin\left(\frac{\lambda}{2d}\right) = \arcsin\left(\frac{12398/8150\ \text{eV}}{6.708\ \text{Å}}\right) \approx 13.107^\circ, \quad (1)$$

where λ is the wavelength of the x-rays, $2d = 6.708$ Å is the spacing of the graphite crystal, and 12398 is a conversion factor factor from eV to Å.

An example of the measured SAXS signal reflected by the HAPG mirror is shown in Fig. 4. The direct XFEL beam with part of the SAXS signal propagates downstream between the mirrors and is shown in Fig. 5 as measured directly by a Timepix detector.

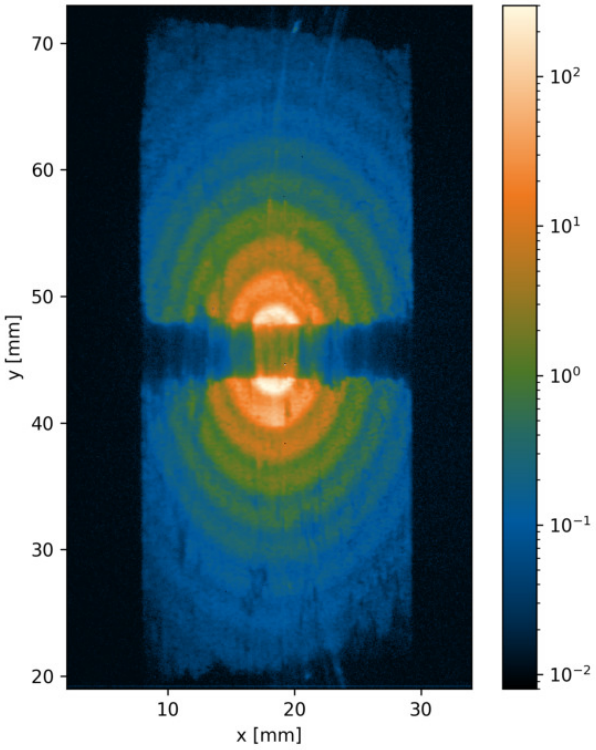

FIG. 4. Scattering pattern from 80 nm SiO_2 nanospheres as reflected by the HAPG mirror and detected by the Jungfrau detector.

IV. SIMULATION

The instrument was designed and benchmarked using the x-ray spectroscopic raytracing code *mmpxrt*[9], which comes with detailed and tested support of mosaic crystals. An extension of the code to easily handle the geometry of this instrument was coded and is included within the distribution package of

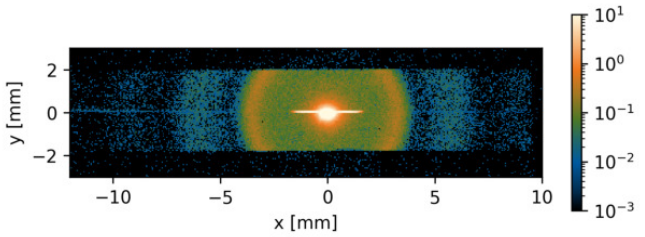

FIG. 5. Part of scattering pattern of 80 nm SiO_2 nanospheres with the direct XFEL beam propagating through a gap between the crystals, detected downstream from the mirror.

the code as *mmpxrtSAXS.py*. For interested users, the latest version of this extension and the input files generating simulations in this paper are available upon request to the author. The geometry of the simulation closely follows the experimental geometry described in thevious previous section. The typical simulation case generates 10^7 monoenergetic rays originating at TCC with isotropic angular distribution passing into an area slightly larger then the crystal surface. The reflection of each ray on the crystal is calculated by taking into account the random nature of the mosaic structure, and an intersection with the detector plane is obtained. Each run can take tens of minutes on an average PC with multi thread capabilities.

The following paragraphs present results of the simulations which were not compared to the experiment. The results, which were compared to the experiment are presented in the next section.

A. Geometrical transformation

Due to its geometry, the curved mirror deforms the scattering pattern. It is not trivial to exactly geometrically describe this deformation (transformation). The raytracing simulation was used to calculate this deformation numerically. To a certain precision, it is possible to approximate the relation between the horizontal and vertical scattering angles $2\theta_X$ and $2\theta_Y$ (in units of *mrad*) and the horizontal and vertical position on the camera x and y by a simple quadratic model. For clarity, the geometry of the setup as well as definitions of the variables are shown in Fig. 6. The geometrical transformation for the particular setup described in this paper can be modelled as follows:

$$\begin{aligned} 2\theta_Y &= 0.174 + 0.677y \\ 2\theta_X &= 0.128 + 1.002x - 5.35\times10^{-3}x^2. \end{aligned} \tag{2}$$

To first order, this shows that a diffraction ring would be deformed to an ellipse with aspect ratio of 0.68. This model, however, does not provide exact results. Figure 7 shows the absolute value of the difference between the numerical solution and this model as a function of position on the detector. It can be seen that the largest difference of 0.2 mrad is in the corner of the mirror furthest from the beam axis, which is at coordinates (0,0). However, for the comparison with experiment shown later, the detected signal was not extended beyond $2\theta = 8$ mrad, for which the deviation would be below 0.05 mrad. In general, the simple model can be used for most cases, but one has to be aware of its limitations. If higher precision is needed, then a matrix with the exact numerical conversion from (x,y) to $(2\theta_X, 2\theta_Y)$, as provided by the code, should be used. Such an approach was used in later analysis in this paper.

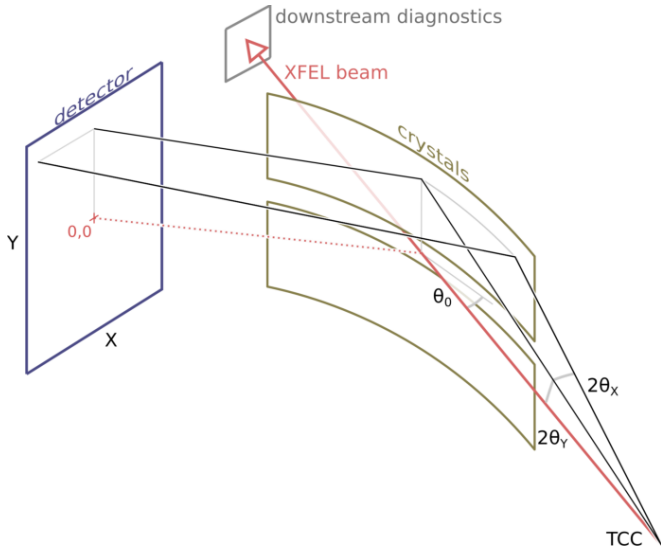

FIG. 6. The geometry of the instrument. The scattering angles at the target are denoted as $2\theta_X$ and $2\theta_Y$, while the Bragg angle on the crystal is labeled θ_0, or eventually θ. Note that these 2θ and θ are different variables, this slightly confusing notation is used due to the well established conventions in both fields of scattering and spectroscopy.

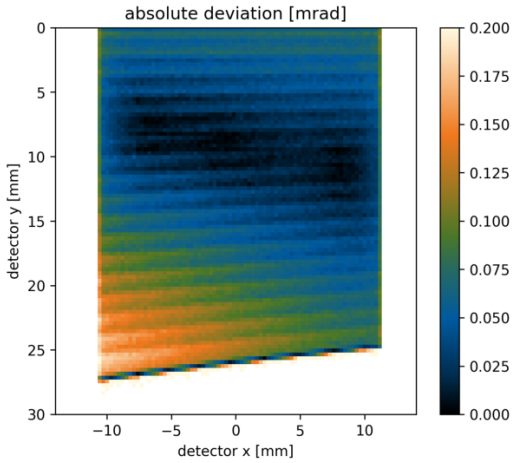

FIG. 7. The angular deviation of the quadratic model from the exact raytracing simulation as a function of a position on the detector.

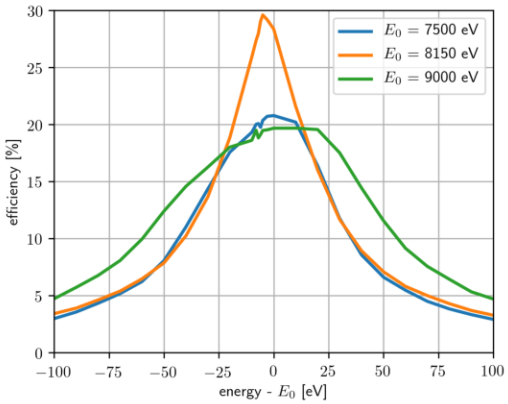

FIG. 8. Demonstration of the acceptance bandwidth of the mirror with a radius $r = 5.5$ m. Each curve shows the efficiency of reflection of a monochromatic beam with a given deviation from the central energy E_0. This energy corresponds to the central Bragg angle θ_0, i.e., the curves differ by a rotation of the mirror.

B. Accepted bandwidth

The bandwidth accepted and reflected by the mirror is controlled by the mosaicity and geometry of the instrument. It is well described by the decrease of the efficiency of the setup for energies different from the central energy. The efficiency in the simulation is defined as the ratio of the reflected rays to the total number of generated rays, multiplied by the theoretical reflectivity of the crystal, which was taken as 45%. Figure 8 shows the efficiency as a function of difference of the x-ray energy from the central energy of the setup E_0. This E_0 denotes the energy corresponding to θ_0, i.e. the three shown cases differ from each other only by a slight rotation of the crystal. All cases use the radius of curvature of the crystal $r = 5.5$ m, which is optimized for $E_0 = 8150$ eV and therefore the efficiency for this energy is the highest. In general, the bandwidth of the instrument is well above 20 eV, which is the typical bandwidth of the XFEL beam. This bandwidth does not decrease when the crystal is used in a non-optimal geometry, but the overall efficiency drops slightly. In the shown cases, it dropped from 30% to 20% when the energy deviation was more than 500 eV from the optimal one.

V. EXPERIMENTAL RESULTS

This section presents various aspects of the instrument using experimental results, demonstrating its performance parameters and the predictive capability of the simulations.

The first case shows the measurement of the rocking curve, which serves as a detailed characterization of the crystal and benchmark of the code. In the second case, the process of flat fielding is shown and its importance is highlighted. The following case demonstrates how precisely the scattering signal from grating target can be measured. The next subsection shows the beneficial effect of the mirror concerning cleaning the signal from parasitic scattering or beam halo. The last topic remarks on the energies at which the mirror can be used and how to further extend its usability.

A. Rocking curve measurement

The rocking curve (RC) shows the reflectivity of photons with given energy as a function of incidence angle on the crystal. It is an extremely important function which defines the scattering properties of the element and therefore its understanding is crucial to be able to interpret the data from the instrument.

The rocking curve of the crystals was measured using two different methods. The first method with direct beam reveals the intrinsic properties of the HAPG layer, while the second one with a SAXS sample provides a more robust experimental measurement and is well suited to be used to align the instrument.

1. RC measurement with direct beam

In this measurement, the XFEL beam was significantly attenuated (the transmission of the attenuators was $\approx 10^{-5}$) and the crystal was moved vertically up so that the beam was reflected directly from the surface of the bottom crystal. The data were taken while the crystal was being rotated within a range of about 3°. Figure 9 shows the images of the beam on the detector for various crystal rotations and therefore various incidence angles. The setup which provided the strongest reflection is labeled as 0.0°, and is assumed to have $\theta = \theta_0 = 13.1°$. It is seen that the signal retains its horizontal dimension of roughly 200 μm, but in the vertical dimension it gets significantly larger and even splits into several fragments. In the figure, each subfigure is normalized so that the overall decrease of intensity is not seen. The splitting and irregularities are ascribed to the non-homogeneous nature of the crystalline layer.

To understand the vertical extension of the signal, it is useful to look into the ray tracing simulations. The result is presented in Fig. 10 and shows the detected image from simulations where the parallel beam is hitting a single spot on a flat HAPG mirror. The same effect of broadening of the signal with increasing deviation from the central θ_0 (white numbers) is seen. For each incoming ray it is assumed there is a set of crystallites present in the crystal which is able to reflect it. Any crystallite with proper angle with respect to the incoming beam can reflect the ray. Those 'suitable' crystallites form a distribution with a range of angles to the crystal normal, denoted as φ, and with probability distribution function $p(\varphi)$ which are randomly selected by the code to be reflecting. These distributions for three different incidence angles are shown in Fig. 11. It can be clearly seen that as θ deviates from θ_0, this distribution gets broader, causing the reflected beam to be more divergent and produce a vertical streak on the detector.

The angle φ is the deviation of the crystallite normal from the crystal normal in the vertical direction. This means, that

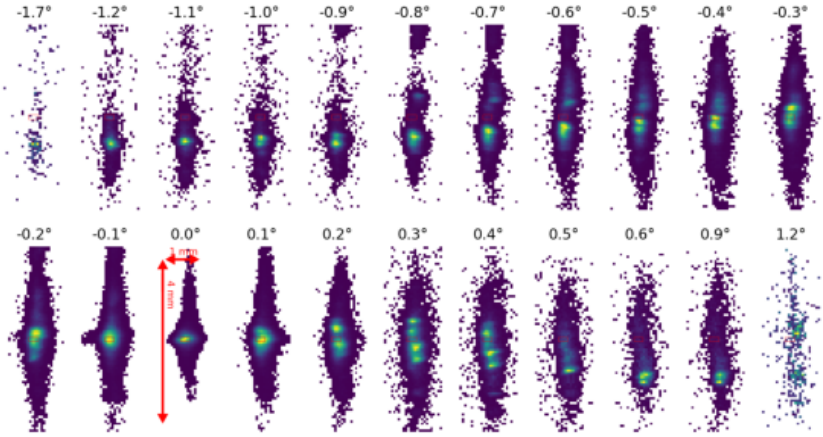

FIG. 9. Reflection of the XFEL beam directly from the surface of the HAPG crystal as a function of incidence angle's deviation from the central Bragg angle. Only pixels with values >0.1% of the maximum in each subfigure are shown.

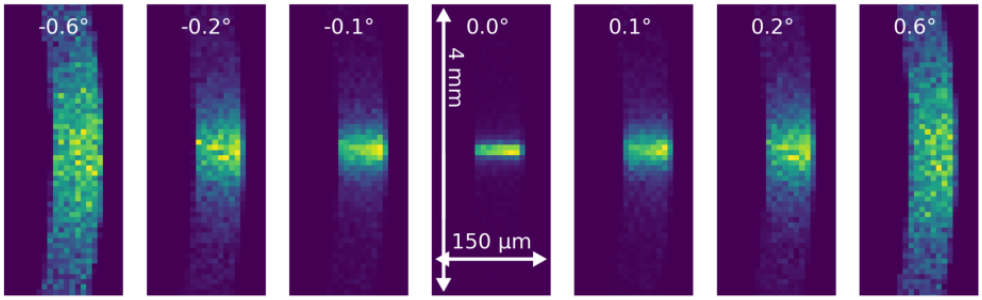

FIG. 10. Simulation of the reflection of the XFEL beam from the surface of the HAPG crystal as a function of incidence angle deviation from the Bragg angle. Each subfigure is normalized.

the originally horizontal ray is vertically reflected by the angle 2φ. Figure 11 shows the probability of finding the crystallite with the orientation described by φ and photon incidence angle θ. It is seen that for $\theta = \theta_0$, this function has a narrow peak with width corresponding to the mosaicity. If θ is further from this optimal condition, the probability (and therefore reflectivity) significantly drops, but it also forms a much broader peak. This broadening is seen in both experimental (Fig. 9) data and the theoretical (Fig. 10) model. The effect bears a large significance, showing that if the mirror is not used in the optimal incidence angle, the instrument loses not only efficiency, but also angular resolution.

The results and issues with this rocking curve measurements are shown in Fig. 12. The blue points show the detected intensity integrated over the whole signal area. The curve is strongly asymmetric with a width of more than 0.5°. It contains a strong plateau extending up to -0.8°. Looking at the data in Fig. 9, this plateau is caused by a reflection directed significantly below the original reflection point (marked by a red rectangle). This could be explained by either a crystallite, or a section of the crystal, pointing downwards in the tested region. For angles above +0.2°, it can be seen that the reflection pattern is significantly fragmented. Both these observations leads us to the conclusion that the tested region was too small to actually measure the mosaicity; rather the reflection from only a few crystallites was observed. Another explanation, however, is that there might be some halo around the XFEL beam, or parts of the beam at slightly different angles (for example from scattering a few meters upstream), and these parasitic rays could produce contamination of the signal. To overcome this, we have implemented another method of evaluation: the orange points in Fig. 12 show the intensity at the position where only the main reflection was originally observed (100×200 µm, marked with red rectangles in Fig. 9). This curve is now significantly closer to the expected 0.1° mosaicity, which lends credence to the explanation of parasitic scattering. However, the wing at negative angles is still present. The green curve shows the same quantity evaluated from the ray tracing simulations. Apart from the wing, the agreement is reasonable. Nevertheless, this method proved itself to be not suitable for mosaicity estimation.

Figure 9 shows images of the diffracted beam for vari-

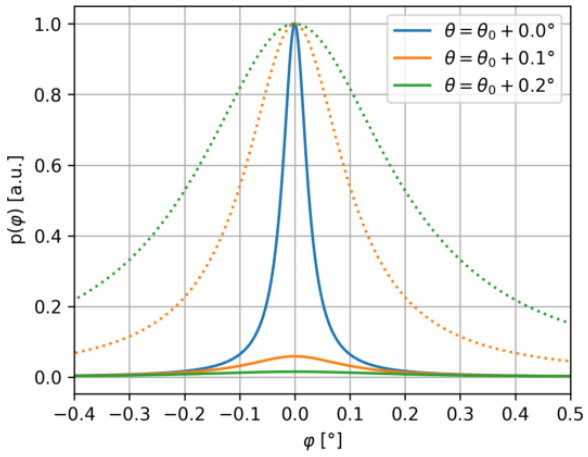

FIG. 11. Probability of reflection as a function of crystallite tilt φ for various incidence angles θ of the ray on the crystal.

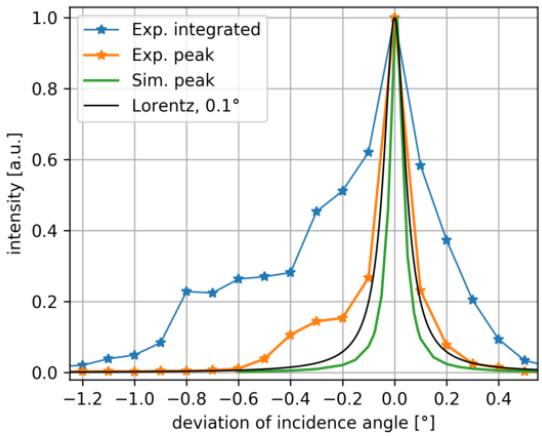

FIG. 12. Rocking curves measured with the direct XFEL beam.

ous crystal rotations (rocking curve positions) measured at the (002) reflection. This data can be transformed into a 3-dimensional reciprocal space map given by the intensity distribution on the detector $I_{3D} = f((i,j),\Delta\theta)$, where $f(i,j)$ is the counted intensity on the given detector pixel and $\Delta\theta$ the deviation from the Bragg peak position. Defining a center peak position (i_0, j_0) for the θ_0 position (i,j) can be recalculated into out-off-plane (coplanar) and in-plane (non-coplanar) diffraction angles $(2\theta, \nu)$ using a simple linear extrapolation. θ_0 and 2θ are lying in one plane and ν in a plane rotated by 90°, the in-plane incidence angle is to be assumed as zero; the coplanar plane is perpendicular to the almost flat sample surface. Therefore, the intensity distribution in reciprocal space can be given as follows:

$$I_{3D}(qx, qy, qz) = I_{3D}((i,j),\Delta\theta); \tag{3}$$

with

$$qx = \frac{2\pi}{\lambda}(\cos(\nu)\cos(2\theta - \theta_0) - \cos(\theta_0)) \tag{4}$$

$$qy = \frac{2\pi}{\lambda}(\sin(\nu)\cos(2\theta - \theta_0)) \tag{5}$$

$$qz = \frac{2\pi}{\lambda}(\sin(2\theta - \theta_0) + \sin(\theta_0)) \tag{6}$$

Assuming a certain degree of mosaicity and almost no lattice constant variations of the HAPG mirror graphite, the intensity distribution around the reciprocal (002) lattice point at $Q(002)$ is approximately constant. Figure 13 shows this 3D map, with a sharp peak along the qz direction, whereas the intensity is smeared out along qx, qy showing a significantly wider distribution perpendicular to the crystal surface due to the mosaicity.

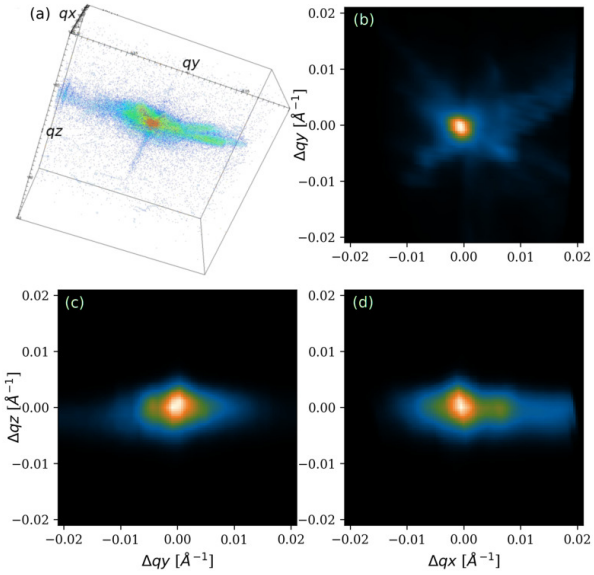

FIG. 13. Reciprocal space map of the reflection, the 3D view (a) and its projections onto three planes (b-d).

2. *RC measurement on nanospheres*

The second method to measure the rocking curve relied on measuring the intensity of a scattering pattern. The experiment was setup to measure the SAXS signal from 80 nm SiO_2 nanospheres (as in Fig. 4), and the integrated intensity of the signal was measured. This method is obviously more stable compared to the previous one since it provides information about the integral performance of the crystals. The rocking curves for both crystals are shown in Fig. 14. They are offset by about 0.08° from each other due to slightly different alignment of each crystal. The curves are fitted with a Lorentzian curve, which provides the FWHM of 0.095° and

0.100° for the upper and lower crystals, respectively. This measurement is suitable to be used at the beginning of each future experiment to find the optimal conditions for crystal operation.

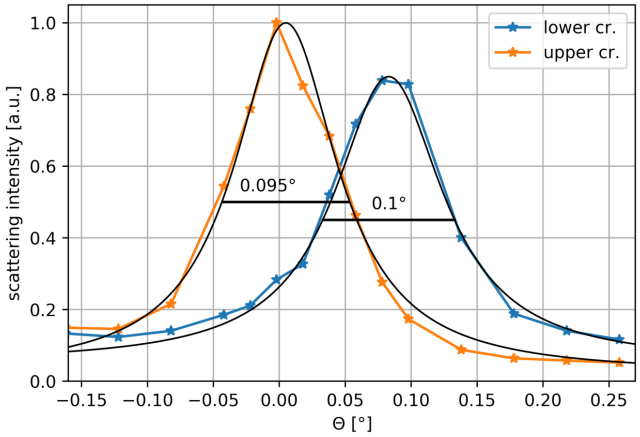

FIG. 14. Intensity of fscattering from 80 nm SiO_2 nanospheres as a function of crystal rotation angle.

B. Flat fielding

It is well known that the reflectivity of HAPG crystals can significantly vary on small scales in a grainy pattern.[10] If an evaluation were not to take that into account, it could cause a strong variation in the measured data especially for scattering on gratings, where small peaks are most likely reflected from single grains on the crystal. For these measurements, a very precise flat fielding has to be made. As the gratings can have a size of less then 1 µm, we do not believe that having a separate map of the reflectivity and applying this map to a given setup would yield the needed precision. Therefore, we have performed a flat fielding directly under experimental conditions, with an identical setup as the real measurement. Several scattering targets were used to produce an intense, broad, and predictable radiation pattern. The scattering pattern of 20 nm SiO_2 nanospheres proven itself to be the best solution.

Figure 15a) shows the raw detected data. It is seen that the diffraction ring is deformed to an ellipse-like shape, and that the reflection from the bottom crystal is stronger due to its better alignment. The data is geometrically converted to the photon divergence angles $2\theta_X$ and $2\theta_Y$, as described in Sec. IV A, and the result is shown with a logarithmic color scale in subfigure (b). The white circle shows the expected scattering of 20 nm nanospheres.

The flatfield data is radially averaged for each crystal, and then divided by this radial average. The result is shown in the pane (c). Additional corrections are made, such that the regions which exhibit too low (probably due to crystal damage) or too high (parasitic signal) values are omitted for the radial average and the division is made again with the finer signal.

As this process is very sensitive to exact positional and rotational alignment of the camera, the variables corresponding to these uncertainties had to be fine tuned. This was done in a way that a series of flat fields were generated while varying those parameters (horizontal and vertical offset of the camera and horizontal rotation angle) and the parameters which provided the flat field containing the smallest traces of the signal were selected as the best ones.

The flat field data shown in Fig. 15 c) are later used to correct other experimental data. The fact that the bottom crystal was in the optimal alignment translates to the observation, that the bottom part of the flat field shows much higher graininess due to the higher resolution of the crystal - reflecting its real structure. The top part is, on the other hand, much smoother due to lower resolution of the misaligned crystal.

C. Scattering from nanospheres

The performance of the mirror and of the flat fielding is demonstrated through scattering from 80 nm SiO_2 nanospheres. Only results from the top crystals are evaluated. The data after geometrical conversion, its corresponding flat field, and the flat fielded data are shown in Fig. 16 a, b and c, respectively. It can be seen that the flat fielding process significantly increases the quality (smoothness) of the data. The white regions in the flat fielded data correspond to regions where the flat field is not available. These are either regions with too low reflectivity, which we consider as damage to the surface, or regions where the parasitic signal dominated the flat field. The radial average of the data is in Fig. 16 d). This signal was compared with the analytical model of hard spheres with 80 nm diameter calculated by the SasView code[11], and with a complementary measurement of direct SAXS. This measurement was performed by putting the detector in the direct XFEL beam to observe the part of the scattering pattern going through the gap between the crystals, therefore it shows significantly worse signal to noise ratio and fewer diffraction rings. Nevertheless, at the peak at ≈ 0.15 nm^{-1} it is seen that the direct measurement provides a slightly better resolution compared to the measurement with the mirror.

D. Scattering from a grating

The scattering from a silicon grating with period 200 nm was selected to demonstrate the performance of the instrument. Similar gratings are commonly used in laser-plasma interaction experiments.[3]

The measurement was performed with the identical setup as the flat field, and the identical procedure was done to geometrically convert the data to divergence angles. Figure 17 (a) shows the grating scattering pattern, and (b) the relevant flat field. The grating was rotated by approximately 45° with respect to the horizontal plane in order to rotate the scattering. This way the signal avoids the horizontal gap between the crystals, as well as the potential vertical parasitic scattering (described in Sec.V E).

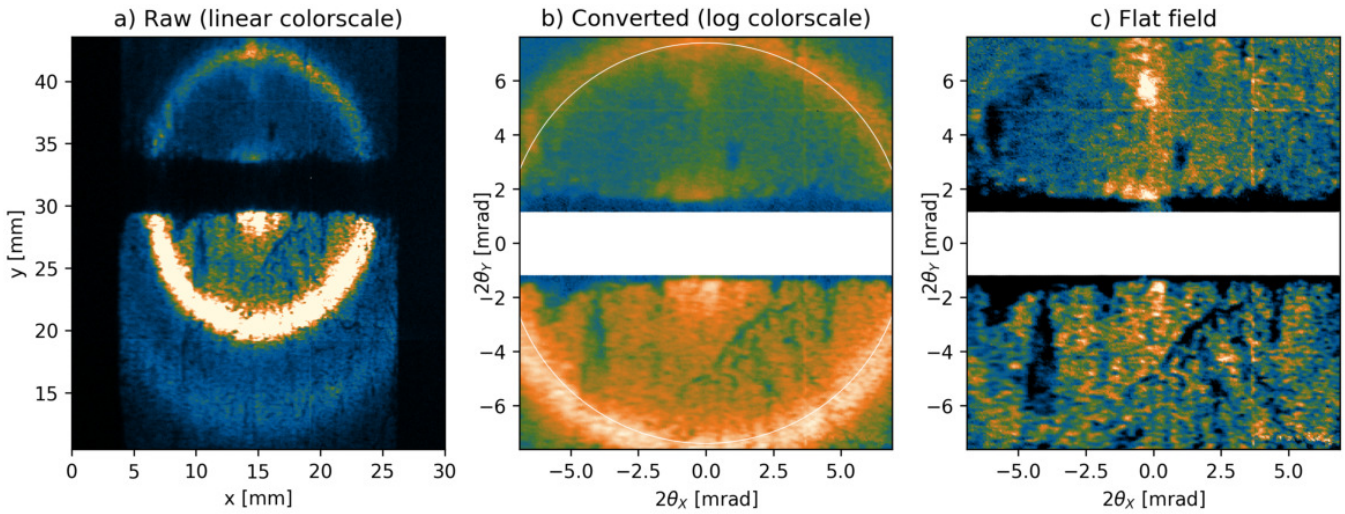

FIG. 15. Illustration of data processing to obtain a flat field from 20 nm SiO_2 nanospheres. a) Raw data as measured on the detector. b) The same data after geometrical correction, the white line shows expected scattering ring with $2\theta = 7.4$ mrad. c) Flat field obtained from this data.

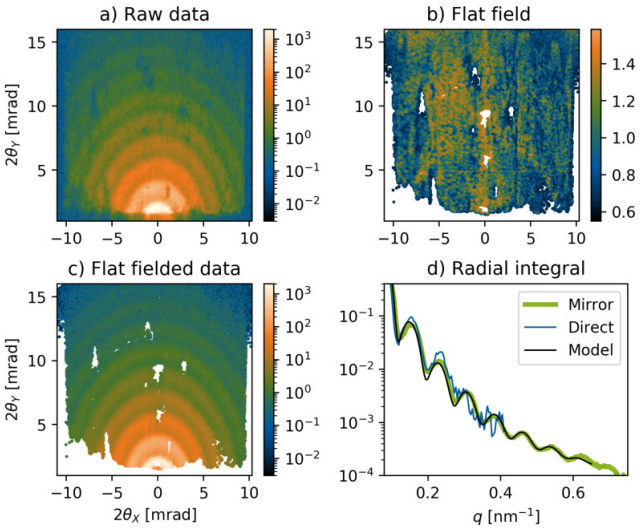

FIG. 16. Scattering signal from 80 nm diameter nanospheres. The detected signal (from Fig. 4) is geometrically transformed (a), divided by the flatfield (b) to form the clean data (c). This is radially averaged and compared to a direct measurement of the same target and an analytical model (d).

To obtain the number of photons detected in each scattering peak, the signal within the small square shown in Fig. 17a) was integrated. The background was estimated for each peak individually as the mean intensity in the region between the larger and smaller rectangles. This background was then subtracted from the signal, and since the Jungfrau detector provides energy calibrated data, the absolute number of detected photons can be obtained. This number is written in the figure next to each peak.

To perform the flat fielding, the signal intensity was integrated over a significantly smaller region of the flat field data (squares in Fig. 17b); the size of this region corresponds to the size of the scattering peak as it was impinging the mirror. Its larger footprint on the detector is caused by its divergence due to the distortion on the mirror. This small region, however, leads to relatively low photon counts, which increases the uncertainty in the resulting peak intensity.

The resulting peak intensity is obtained by dividing the number of photons in the peak by the relevant flat field. These values are shown in Fig. 18 for both the upper and lower crystal. These two sets are not normalized: the fact that the intensity in the peak agrees within the error bars is a real measured property showing that the scattering pattern is symmetric. Since the scattering from a grating should be symmetric, with possible asymmetry due to imprecise manufacturing on the order of maximally a few percent, these results are taken as proof that the flat fielding and correction of data works properly even in such difficult conditions where one crystal was aligned to 0.08°away from its optimal position, decreasing its efficiency by approximately a factor of three.

The error bars in Fig. 18 come from the Poisson statistics of photon counting, i.e., they are caused by insufficient signal. Therefore the data from the lower crystal (orange) exhibits a lower uncertainty due to the approximately three times higher signal. The contribution of the signal and flat field to this uncertainty is in this case comparable, meaning that in order to improve the data quality, signal levels in both data sets would have to be increased.

E. Signal cleaning

The mirror is designed to reflect the radiation coming from TCC and therefore it cleans the detected signal originating from other sources. This is another advantage of this setup compared to typical experiments, where the SAXS was measured directly without any reflecting element. The XFEL

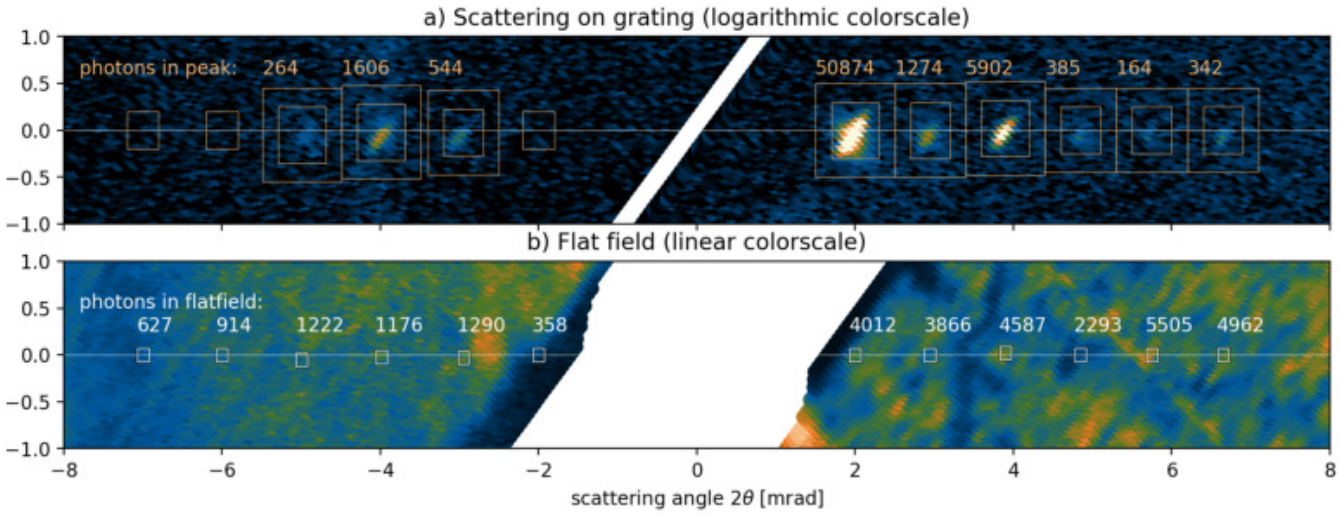

FIG. 17. a) Detected scattering signal from a 200 nm silicon grating, after geometrical correction. Smaller rectangles show the area where photons for each peak were integrated, larger ones the area where background was estimated. Numbers show the number of photons in the peak after background subtraction. b) flat field data processed from scattering from 80 nm nanospheres, processed the same way as the grating data. White squares show the area where the flat field value was taken for each peak, numbers correspond to number of photons in that region. Left and right parts have different color-scales for clarity.

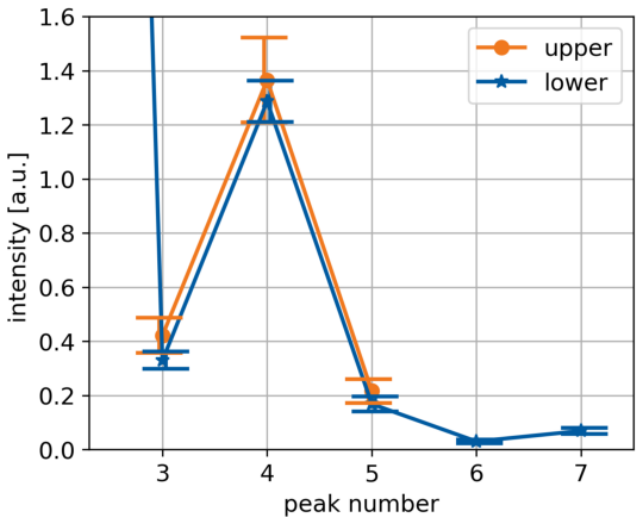

FIG. 18. Intensity of peaks scattered off a 200 nm grating.

beam can in general contain an unwanted halo formed from a collimated beam with much larger radius and very low intensity, scattering from slits upstream in the beampath, or a larger higher harmonic content. The mirror will significantly decrease the contribution of these unwanted rays. Due to the Bragg condition, the higher harmonics of the beam are also reflected, but with significantly lower reflectivity. According to[10], the reflectivity of 40 µm thick HAPG for 9 keV radiation in the first order is approximately 45%, while for the second harmonics in the second order it is only 5% and for third harmonics in the third order it goes down to 0.7%.

The geometry of the instrument is set up so that rays originating from TCC have incidence angles close to the Bragg angle. Any rays which are parallel to the experimental axis, but horizontally offset, or rays which are scattered from a different location than TCC, could deviate from this condition and might not be reflected (or reflected with a lower probability). Such situations were modeled by the raytracing code. Figure 19 (a) shows the simulated detected pattern of isotropic scattering originating at TCC, (b) 0.5 m upstream of TCC (b), and (c) 3 m upstream of TCC. It can be observed that the mirror reflects scattering from TCC almost homogeneously, but the further upstream the source is, the narrower the vertical stripe is.

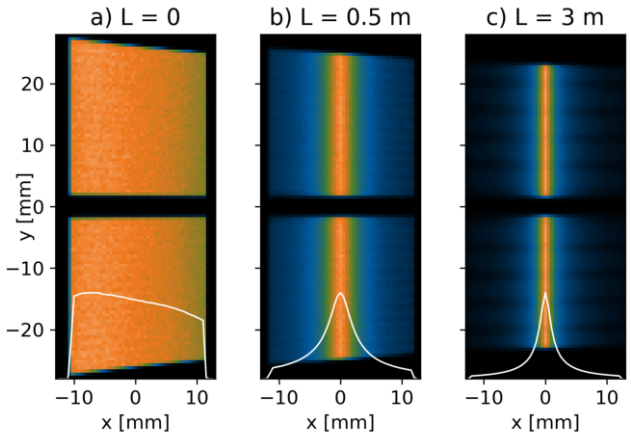

FIG. 19. Simulated detected signal where the homogeneous diffuse scattering target is at TCC (a), 0.5 m further upstream (b), and 3 m upstream (c). The white line shows the mean over the vertical extent of the signal.

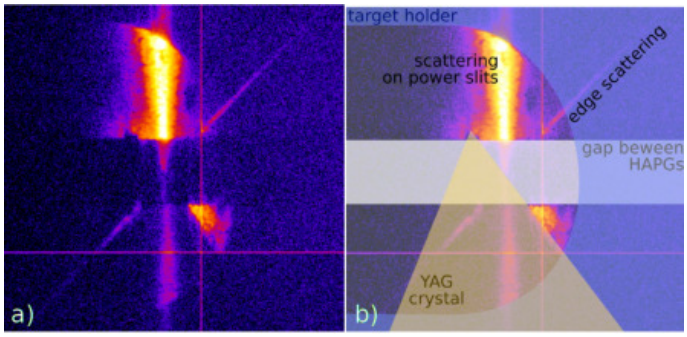

FIG. 20. Measured signal with radiation source located 3 m upstream from TCC, combining edge scattering on the YAG crystal with a radiography of the target.

This scenario was demonstrated experimentally. In one of the shots, the clean up slits located approximately 3 m upstream from TCC were slightly closed to scatter the beam, providing a source with strong divergence. The beam at TCC was scattered by the edge of the YAG crystal. The recorded image is shown in Fig. 20 a), the subfigure (b) contains a drawing explaining the location of various components. The figure contains a clear diagonal line which originates from scattering from the sharp edge of the YAG crystal. The rest of the signal provides a radiography of the target and target holder backlit by the upstream scattering. The important feature is that this radiography is constrained to a vertical area therefore it is not disturbing the scattering signal.

F. Usability at various energies

The radius of curvature of the mirror and its distance from TCC defines the energies at which the mirror can be used (the *optimal energy*). If a mirror is used for energies other than this optimal energy, then the central Bragg angle θ_0 needs to be adjusted. However, an inappropriate radius of curvature will cause rays with certain horizontal declination $2\theta_X$ to not fulfill the Bragg condition. The energy range for which each mirror can be used is not easy to quantify. In Fig. 21 we present two experimental results, subfigure (a) shows the scattering of a beam with $E = 8150$ eV from 20 nm nanospheres, i.e. the optimal energy for the given setup. It can be seen that basically the whole area of the crystal is well reflecting. The white line shows the horizontal lineout of the data and is indicative of the reflectivity of the crystal. Subfigure (b) shows data where the XFEL energy was set to $E = 9500$ eV and the crystal was rotated by 1.86°to adjust θ_0 to this new energy. The horizontal lineout shows that now only the central part of the crystal is reflecting, and the efficiency drops significantly towards the edges. This efficiency curve has a FWHM close to 10 mm, compared to about 20 mm for $E = 8150$ eV.

To study this effect in simulations, we have chosen the FWHM of the horizontal signal lineout with an isotropic source as the figure of merit. The results are shown in Fig. 22. The blue line represents the setup using a crystal with radius

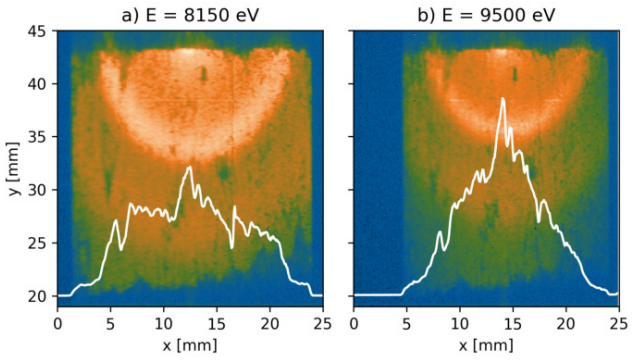

FIG. 21. Detected pattern from 20 nm nanospheres at different XFEL energies. The white line represents the horizontal mean of the data, showing that at the non-optimal case with $E = 9500$ eV, the efficiency drops towards the edges of the instrument due to too strong mirror curvature.

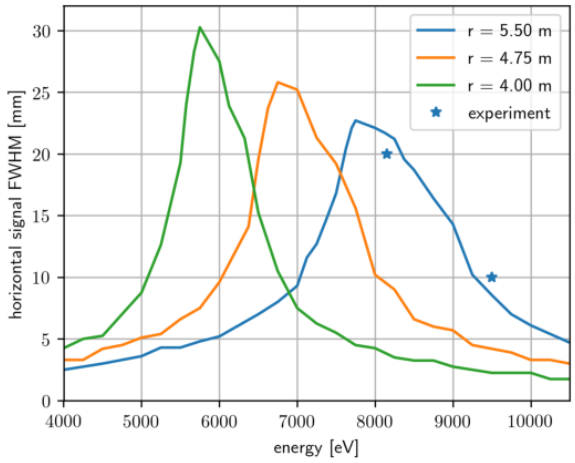

FIG. 22. Simulated widths of the detected signals for various XFEL energies for three different radii of the mirror. The points represent the results from Fig. 21.

$r = 5.5$ m. It can be seen that this crystal is usable for energies between roughly 7500 and 9000 eV. The other lines show that a set of crystals with three radii could effectively cover the energy range between 5500 and 9000 eV. The blue dots are the values estimated from Fig. 21, showing a good agreement to the simulation.

VI. SUMMARY AND CONCLUSION

We have designed, fabricated, and commissioned the *SAXS mirror*, a novel tool to measure the small angle x-ray scattering (SAXS) signal in harsh laser plasma interaction experiments. This instrument was commissioned in an experiment

at the HED instrument of the European XFEL and is available there for further use. With the current curvature of the mirror it can be used to measure scattering at energies between roughly 7500 and 9000 eV, however, it is possible to employ mirrors with different radii of curvature to cover different energies. In the basic setup, the mirror provides a bandwidth of roughly 30 eV, an angular resolution of 0.2 mrad, and works at scattering angles from 2 to 30 mrad providing a q range of roughly 0.06 - 1 nm^{-1}. This q range can be extended in both directions if needed. The lower range is limited by the positional stability of the x-ray beam, the higher by the size and vertical position of the mirror.

In general, the principles of this instrument can be used to measure SAXS in various configurations and facilities. The instrument is planned to be used in combination with an optical-laser irradiated target in the future and its performance for this real case scenario will be investigated.

VII. ACKNOWLEDGMENTS

This research was supported by the Helmholtz Association under the grant no. VH-NG-1338. The authors are indebted to the HIBEF UC for the provision of instrumentation and staff that enabled this experiment. This work benefited from the use of the SasView application, originally developed under NSF award DMR-0520547. SasView contains code developed with funding from the European Union's Horizon 2020 research and innovation programme under the SINE2020 project, grant agreement No 654000. We acknowledge European XFEL in Schenefeld, Germany, for provision of X-ray free-electron laser beamtime at High Energy Density scientific instrument and would like to thank the staff for their assistance.

VIII. DATA AVAILABILITY

The data that support the findings of this study are available from the corresponding author upon reasonable request.

[1] M. Rödel, *Coherent X-ray Diffraction of Laser-driven Matter*, Ph.D. thesis, Technische Universität Dresden (2020), to be submitted.
[2] B. R. Pauw, "Everything SAXS: small-angle scattering pattern collection and correction," Journal of Physics: Condensed Matter **25**, 383201 (2013).
[3] T. Kluge, M. Rödel, J. Metzkes-Ng, A. Pelka, A. L. Garcia, I. Prencipe, M. Rehwald, M. Nakatsutsumi, E. E. McBride, T. Schönherr, M. Garten, N. J. Hartley, M. Zacharias, J. Grenzer, A. Erbe, Y. M. Georgiev, E. Galtier, I. Nam, H. J. Lee, S. Glenzer, M. Bussmann, C. Gutt, K. Zeil, C. Rödel, U. Hübner, U. Schramm, and T. E. Cowan, "Observation of ultrafast solid-density plasma dynamics using femtosecond x-ray pulses from a free-electron laser," Phys. Rev. X **8**, 031068 (2018).
[4] T. Tschentscher, C. Bressler, J. Grünert, A. Madsen, A. Mancuso, M. Meyer, A. Scherz, H. Sinn, and U. Zastrau, "Photon beam transport and scientific instruments at the european xfel," Appl. Sci.. Applied Sciences (2017).
[5] T. Metzger, I. Kegel, R. Paniago, A. Lorke, J. Peisl, J. Schulze, I. Eisele, P. Schittenhelm, and G. Abstreiter, "Shape, size, strain and correlations in quantum dot systems studied by grazing incidence x-ray scattering methods," Thin Solid Films **336**, 1 – 8 (1998).
[6] T. Kluge, M. Bussmann, H.-K. Chung, C. Gutt, L. G. Huang, M. Zacharias, U. Schramm, and T. E. Cowan, "Nanoscale femtosecond imaging of transient hot solid density plasmas with elemental and charge state sensitivity using resonant coherent diffraction," Physics of Plasmas **23**, 033103 (2016), https://doi.org/10.1063/1.4942786.
[7] H. Legall, H. Stiel, M. Schnürer, M. Pagels, B. Kanngießer, M. Müller, B. Beckhoff, I. Grigorieva, A. Antonov, V. Arkadiev, and A. Bjeoumikhov, "An efficient X-ray spectrometer based on thin mosaic crystal films and its application in various fields of X-ray spectroscopy," Journal of Applied Crystallography **42**, 572–579 (2009).
[8] A. Y. Faenov, S. A. Pikuz, A. I. Erko, B. A. Bryunetkin, V. M. Dyakin, G. V. Ivanenkov, A. R. Mingaleev, T. A. Pikuz, V. M. Romanova, and T. A. Shelkovenko, "High-performance x-ray spectroscopic devices for plasma microsources investigations," Physica Scripta **50**, 333–338 (1994).
[9] M. Šmíd, X. Pan, and K. Falk, "Raytracing code for x-ray mosaic crystal spectrometers," Computer Physics Communications , submitted (2020).
[10] M. Gerlach, L. Anklamm, A. Antonov, I. Grigorieva, I. Holfelder, B. Kanngießer, H. Legall, W. Malzer, C. Schlesiger, and B. Beckhoff, "Characterization of HAPG mosaic crystals using synchrotron radiation," Journal of Applied Crystallography **48**, 1381–1390 (2015).
[11] "Sasview," available online (2020), http://www.sasview.org/.